Bessel-beam Grueneisen relaxation photoacoustic microscopy with extended depth of field

Junhui Shi
Lidai Wang
Cedric Noordam
Lihong V. Wang

SPIE.

Bessel-beam Grueneisen relaxation photoacoustic microscopy with extended depth of field

Junhui Shi,[a,†] **Lidai Wang,**[a,b,†] **Cedric Noordam,**[a,c] **and Lihong V. Wang**[a,*]
[a]Washington University, Optical Imaging Laboratory, Department of Biomedical Engineering, Campus Box 1097, One Brooking Drive, St. Louis, Missouri 63130-4899, United States
[b]City University of Hong Kong, Department of Mechanical and Biomedical Engineering, 83 Tat Chee Avenue, Kowloon Tong, Hong Kong SAR, China
[c]University of Twente, Optical Sciences, MESA+ Institute for Nanotechnology, P.O. Box 217, 7500 AE Enschede, The Netherlands

Abstract. The short focal depth of a Gaussian beam limits the volumetric imaging speed of optical resolution photoacoustic microscopy (OR-PAM). A Bessel beam, which is diffraction free, provides a long focal depth, but its side lobes deteriorate image quality when the Bessel beam is directly employed to excite photoacoustic (PA) signals in OR-PAM. We present a nonlinear approach based on the Grueneisen relaxation effect to suppress the side-lobe artifacts in PA imaging. This method extends the focal depth of OR-PAM and speeds up volumetric imaging. We experimentally demonstrated a 1-mm focal depth with a 7-μm lateral resolution and volumetrically imaged a carbon fiber and red blood cell samples. © *2015 Society of Photo-Optical Instrumentation Engineers (SPIE)* [DOI: 10.1117/1.JBO.20.11.116002]

1 Introduction

Optical resolution photoacoustic microscopy (OR-PAM), which provides high sensitivity by detecting optical absorption contrasts, has been widely used for imaging biological systems, from single cells to organisms.[1–5] A conventional OR-PAM setup typically excites molecules using a focused Gaussian laser beam, which can have a micron- to submicron-sized focal spot but suffers from limited focal depth. In order to acquire millimeter-thick volumetric images with consistent lateral resolution in the depth direction, we need three-dimensional (3-D) raster scanning to compensate for the short focal depth, which reduces the imaging speed. In comparison, a Bessel beam is essentially diffraction free, i.e., the focal depth can be extended greatly without compromising the focal spot size, which avoids the tradeoff between imaging resolution and focal depth.[6–8] However, Bessel beams have many strong side lobes, which generate ghost signals, limiting their application in optical imaging. Similarly, in photoacoustic (PA) imaging, ultrasound transducers usually have large focal diameters (tens to hundreds of microns), and thus they receive most of the ghost signals from the side lobes of the Bessel beam,[9] which inhibits the direct application of Bessel beams in PA imaging.

Until recently, nonlinear optical techniques, e.g., two-photon excitation in fluorescence microscopy, have been successfully used to suppress the side-lobe effect of Bessel beams and then achieve rapid volumetric imaging with a long focal depth.[10–14] Nonlinear effects exist in PA imaging as well.[15–21] One of them is the Grueneisen relaxation (GR) effect,[20] a thermally induced nonlinear effect that has been explored to improve both the axial and lateral resolution for PAM.[20,21] Here, we utilize the GR effect in Bessel-beam PAM to suppress the side-lobe effect and achieve long-focal-depth volumetric imaging.

2 Methods

GR-PAM employs dual-pulse excitations to obtain nonlinear PA signals.[20] The first laser pulse generates a PA signal and, at the same time, increases the local temperature. The second laser pulse is almost identical to the first laser pulse and excites the same absorber within the thermal confinement time. Owing to the temperature rise induced by the first pulse, the local Grueneisen parameter is increased, and the second PA signal is stronger than the first one. The nonlinear PA signal is the amplitude difference between these two signals and is proportional to the square of the optical fluence, thereby achieving nonlinear effects. Alternatively, we can also realize GR-PAM using a two-step measurement scheme. In the first step, one probe laser pulse generates a PA signal; in the second step, a heating laser is applied before firing the second probe laser pulse. The resulting nonlinear PA signal is the difference of the two signals from the two-probe laser pulse excitations. In this way, the heating laser could be either a continuous-wave (CW) or a pulsed laser, as long as the turn-on time and time delay between the heating and probing fulfill the thermal confinement requirement. In the two-step measurement scheme, the first probe laser pulse generates an initial pressure rise:

$$p_1(x, y) = \Gamma_0 \eta_{\text{th}} \mu_a(x, y) F_1(x, y), \qquad (1)$$

where Γ_0 is the Grueneisen parameter at the initial temperature, η_{th} is the heat conversion efficiency, $\mu_a(x, y)$ is the optical absorption coefficient, and $F_1(x, y)$ is the optical fluence of the probe pulse laser. The PA signal is the spatial integration of $p_1(x, y)$:

*Address all correspondence to: Lihong V. Wang, E-mail: lhwang@wustl.edu.

†These authors contributed equally.

$$PA_1 = k\Gamma_0\eta_{th}\iint \mu_a(x,y)F_1(x,y)dx\,dy, \qquad (2)$$

where k is a coefficient representing the ultrasonic detection sensitivity and is assumed to be spatially invariant within the acoustic focus.

In the second step, after the heating laser is applied, the Grueneisen parameter increases owing to the local temperature rise:

$$\Gamma_2 = [1 + \alpha\eta_{th}\mu_a(x,y)F_2(x,y)]\Gamma_0, \qquad (3)$$

where α is a constant that relates the absorbed energy to the Grueneisen parameter change, and $F_2(x,y)$ is the optical fluence of the heating laser. The initial pressure rise induced by the second probe laser pulse is given by

$$p_2(x,y) = [1 + \alpha\eta_{th}\mu_a(x,y)F_2(x,y)]\Gamma_0\eta_{th}\mu_a(x,y)F_1(x,y). \qquad (4)$$

The corresponding PA signal is

$$PA_2 = k\Gamma_0\eta_{th}\iint \mu_a(x,y)[1 + \alpha\eta_{th}\mu_a(x,y)F_2(x,y)]F_1(x,y)dx\,dy. \qquad (5)$$

Subtracting Eq. (2) from Eq. (5), we obtain a differential PA signal (ΔPA):

$$\Delta PA = k\Gamma_0\alpha\eta_{th}^2\iint \mu_a^2(x,y)F_2(x,y)F_1(x,y)dx\,dy. \qquad (6)$$

When the heating laser and probe laser have the same optical beam profile, then their optical fluences are linearly proportional to each other: $F_2(x,y) = gF_1(x,y)$, where g is a constant depending on the power ratio of these two lasers. This simplifies Eq. (6) to

$$\Delta PA = gk\Gamma_0\alpha\eta_{th}^2\iint \mu_a^2(x,y)F_1^2(x,y)dx\,dy, \qquad (7)$$

which shows a nonlinear dependence on optical fluence, while the signal PA_1 has only a linear dependence as expressed in Eq. (2).

Let the optical fluence follow a Bessel profile:

$$I(r,z) = I_0(z)J_0^2\left(2.4048\frac{r}{r_0}\right), \qquad (8)$$

where $I_0(z)$ is the optical intensity at axial position z, r_0 is the radius of the central lobe, r is the transverse radial coordinate ($r = \sqrt{x^2 + y^2}$), and $J_0(r)$ is the zero-order Bessel function of the first kind. Due to the existence of many side lobes, the point spread function of linear OR-PAM on the transverse plane following the function of $J_0^2(r)$ also has many side lobes. But if we use the nonlinear PA signal ΔPA to form an image, then the point spread function becomes the square of the Bessel beam profile, $J_0^4(r)$. Because the amplitudes of side lobes are much smaller than that of the central lobe, the contribution of the side lobes is reduced by squaring, as has been demonstrated in two-photon Bessel-beam microscopy.[10] The attenuation of side-lobe effects in nonlinear Bessel-beam PAM can also be interpreted as a result of low heating effect of the side lobes due to their low optical fluence. The further away the side lobe is from the central lobe, the less the nonlinear PA signal it contributes.

3 Experimental Setup

Figure 1(a) is a schematic of a Bessel-beam PAM system. The probe laser is a 532-nm diode-pumped solid-state pulsed laser (Innoslab BX2II-E, Edgewave GmbH), which generates 10-ns laser pulses at repetition rates in the range of hundreds of hertz. The heating laser beam, from either a CW laser or a pulsed laser, is combined with the probe laser beam and then spatially filtered by a 50-μm tungsten pinhole. The filtered laser beam has a 3-mm diameter and a near-Gaussian transverse profile. Finally, an axicon lens (Thorlabs AX255-A, 25 mm, 5.0 deg) transforms
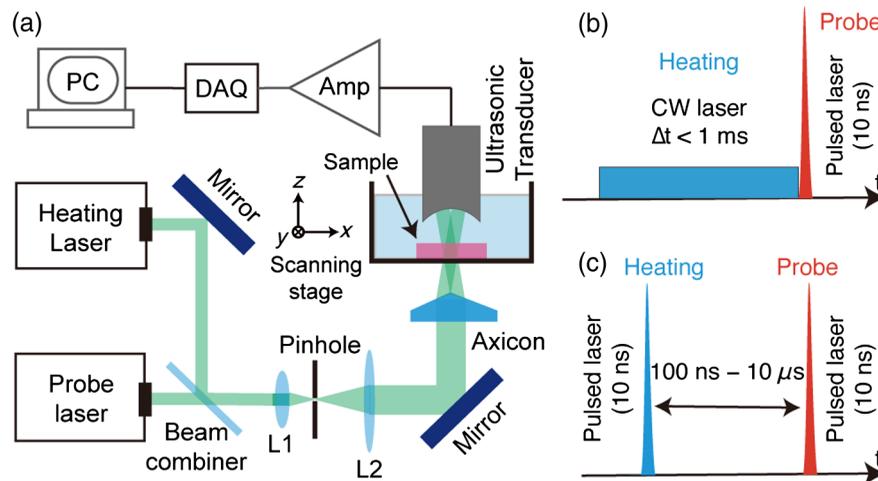

Fig. 1 Schematic of Bessel-beam photoacoustic microscopy (PAM). (a) Experimental system setup. L1, L2: lens. (b) Continuous wave (CW)-heating scheme. A CW laser is used as the heating laser. The heating duration (Δt) of the CW laser must be less than the thermal relaxation time. (c) Pulsed-heating scheme. Both the heating and probe laser beams are pulsed, and the interpulse delay ranges from 100 ns to 10 μs.

the laser beam into a Bessel beam. The sample holder, a petri dish filled with water for ultrasound coupling, is mounted on a 3-D scanning stage (PLS-85, PI miCos GmbH) and it is about 7 mm away from the tip of the axicon lens. When the sample is irradiated by the Bessel beam, PA waves are generated through light absorption and then detected by a custom-made focused ultrasonic transducer (48-MHz central frequency, 80% detection bandwidth, 11.6-mm focal length, and 0.25 NA). The focal zone of this transducer is about 2 mm, encompassing the long focal depth of the Bessel beam. The PA signal from the transducer is further amplified by 40 dB (ZKL-1R5+, Minicircuits) and digitized at 500 MHz using a data acquisition card (ATS9350, AlazarTech). A LabVIEW programmed FPGA card (PCI-7830R, National Instruments) synchronizes the laser triggers, scanner motion, and data acquisition for imaging. A microcontroller (Arduino Due) programs the CW laser TTL trigger and the interpulse delay.

The axicon lens converts a Gaussian beam to a good approximation of a true Bessel beam.[10,22–24] According to Ref. 25, the radius of the central lobe (ρ) is defined as the first zero of the Bessel function: $\rho = 2.40\lambda/(2\pi\beta)$, where λ is the wavelength, $\beta = \sin^{-1}(n \sin \alpha) - \alpha$, α is the axicon angle, and n is the refractive index of the axicon lens material. The depth of field is $L = 0.8w_0/\beta$, where w_0 is the beam diameter of the incident Gaussian beam. In our system, the wavelengths of both the CW laser and pulsed lasers are 532 nm, and the beam diameter of the incident Gaussian beam is 3 mm. The beam profile, measured by a beam profiler (BeamGage, Ophir), as shown in Fig. 2(a), is the transverse intensity profile of the Bessel beam taken at a relative axial position $z = 2$ mm (The axial position at $z = 0$ mm is about 7 mm away from the tip of the axicon lens). The central lobe has a full-width at half-maximum (FWHM) of 6.5 μm, while the side lobes spread widely beyond a 100-μm-diameter circular area. The central lobe diameter varies depending on the axial position relative to the axicon lens. The axial distributions of the central lobe diameter (FWHM) and peak intensity of the central lobes are shown in Fig. 2(b). In the region $z > 0$ mm, the transverse beam profile can be described as a quasi-Bessel beam and the central lobe diameter is around 6 to 7 μm. In the region $z < 0$, i.e., closer to the axicon lens, the central lobe diameter diverges quickly; hence, this region should be avoided for imaging due to its

poor resolution. In practice, the peak intensity is also an important factor, since a low peak intensity not only attenuates the PA signal but also attenuates the heating effect. Therefore, for the Bessel beam shown in Fig. 2, only a 2-mm focal depth $(0 < z < 2$ mm) is used for nonlinear Bessel-beam PAM. This focal depth is much larger than that of conventional Gaussian beams, e.g., the focal depth of a Gaussian beam with the same focal spot size 6 μm at 532 nm is only about 106 μm.

To generate nonlinear PA signals, we employ two schemes. In the first scheme, as illustrated in Fig. 1(b), a CW laser is turned on for a short period of time Δt to heat the sample and then a pulsed probe laser is triggered at the end of the heating. The heating time is within the thermal relaxation time. The pulsed probe laser generates PA signals, whereas the CW laser is only for heating. At each scanning point, we record two PA signals: the first PA signal (PA$_1$) is excited by a single laser pulse without CW laser heating, whereas the second PA signal (PA$_2$) is excited by another laser pulse right after the CW laser heating. Owing to the GR effect, the second PA signal is stronger than the first one, and their amplitude difference is the nonlinear PA signal (ΔPA). Due to its low power (<100 mW in our system) and the thermal confinement of the target, the CW laser is good for heating highly absorptive samples (e.g., carbon fiber, hair, etc.). In the second scheme, both the heating laser and the probe laser are pulsed, as shown in Fig. 1(c). The interpulse delay is a constant ranging from 100 ns to several μs, which is much shorter than the thermal relaxation time. In this scheme, similar to the first scheme, two probe PA signals are recorded with and without the pulsed heating. Their computed amplitude difference is the nonlinear PA signal (ΔPA). The pulsed heating laser, possessing higher pulse energy, provides better heating effect for low absorptive samples but is more expensive than the CW heating laser. In our experiments, we demonstrated the feasibility of both schemes. We employed the first scheme to measure a carbon fiber to quantify the effect of the nonlinear Bessel-beam PAM and then used the second scheme to image red blood cell (RBC) samples.

4 Results and Discussion

In order to quantify the lateral resolution and effective axial focal depth, we imaged a carbon fiber (6-μm diameter) using the nonlinear Bessel-beam PAM system. The thermal relaxation
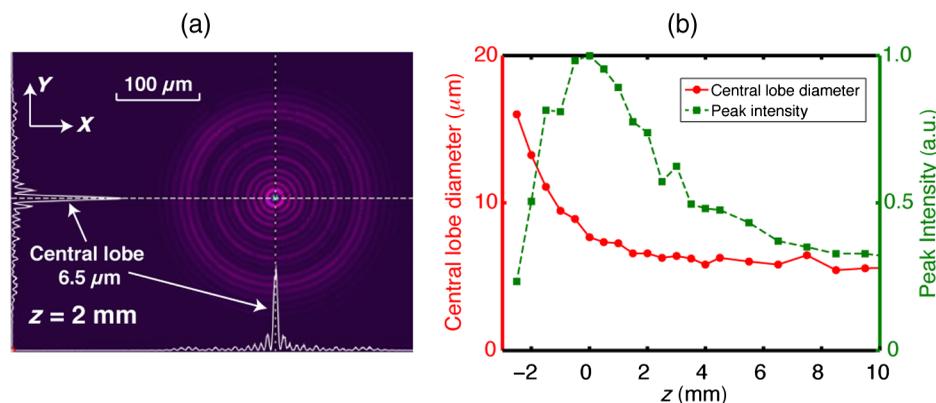

Fig. 2 Bessel beam profile. (a) Transverse intensity profile taken at $z = 2$ mm (at $z = 0$ mm, it is about 7 mm away from the tip of the axicon lens). The central lobe diameter (6.5 μm) is the full-width at half-maximum (FWHM) of the central lobe. White peaks represent intensity profiles along white dashed lines, respectively. (b) Axial distributions of the central lobe diameter (red solid line, Y-axis is on the left side) and peak intensity (green dashed line, Y-axis is on the right side).

time of a carbon fiber immersed in water with a 6.5-μm diameter optical heating spot has been estimated to be 1 ms,[26] so we heated the carbon fiber using a 532-nm CW laser (40-mW power, 300-μs duration, and equivalent heating energy 12 μJ) and excited PA signals using a pulsed laser (10-ns pulse width and 1200-nJ pulse energy). Because the energy distributes almost equally among the central and each side lobe of the Bessel beam, only a small portion of the energy can be absorbed by the thin carbon fiber. The carbon fiber was placed horizontally in the petri dish and immersed in water for coupling and a cross-sectional PA image was obtained by one-dimensional mechanical scanning across the carbon fiber. A typical measured PA amplitude profile across the carbon fiber is shown in Fig. 3(a), where the red line CW_{on} is the enhanced PA image with the CW laser heating, while the blue line CW_{off} is the conventional PA image acquired without laser heating. Both the CW_{on} and CW_{off} images have significant backgrounds, which are produced by the side lobes of the Bessel beam. By taking the amplitude difference between CW_{on} and CW_{off}, we computed the differential PA image ΔPA, which clearly reduces the background and suppresses the side-lobe effect. In Fig. 3(a), the FWHM of ΔPA is about 6.1 μm, which is close to the value of 6.5 μm estimated from the convolution of the carbon fiber cross-section profile and the profile squared of the Bessel beam central lobe. Figure 3(b) shows the lateral resolution at different axial positions. In the region of 0.6 mm $< z <$ 2.2 mm, the FWHM value is around 6.2 μm while it increases quickly for smaller z ($<$0.6 mm, closer to the axicon lens) because the central lobe diameter becomes large, as shown in the Bessel light beam profile in Fig. 2(b). For $z >$ 2.2 mm (further from the axicon lens), the FWHM also deteriorates, since the heating light intensity of the central lobe is attenuated significantly in this region. In summary, the effective nonlinear Bessel-beam imaging region in Fig. 3(b) is about 1.6 mm in which the system maintains a lateral resolution finer than $\sim$7 μm.

Besides the carbon fiber, we also imaged RBC samples, which are relatively low absorptive. Bovine RBCs (Quad Five, Ryegate, Montana) were first fixed with methanol and then mixed with agar gel (1% weight ratio of agarose and water) at 40°C. The volume ratio between the RBC and agar gel was 1 : 500. A single-layer RBC sample was prepared by simply smearing the RBC-agar gel onto a cover glass. A thick-layer (0.5 to 1.0 mm) RBC sample was formed by dropping the gel into a hole in the bottom of a petri dish sealed with a cover glass. Finally, the RBC-agar gel was cooled to room temperature (25°C) to form solid samples. The single-layer RBC sample was used to quantify the side-lobe suppression effect. The thick-layer sample was used to demonstrate the volumetric imaging capability of nonlinear Bessel-beam PAM. To provide sufficient power to heat the highly diluted RBC sample, we exchanged the CW heating laser for a high-power pump laser (Innoslab IS8II-E, Edgewave GmbH, 20-μJ pulse energy) and triggered a probe laser (Innoslab BX2II-E, Edgewave GmbH, 14-μJ pulse energy) to generate PA signals about 300 ns after triggering the heating pulsed laser.

We performed two-dimensional (2-D) raster scanning to image the single-layer RBC sample (actually four separated RBCs) in the agar medium. The regular probe-only PA image PA_1, thermally enhanced PA image PA_2, and the differential PA image ΔPA ($PA_2 - PA_1$) are displayed in Figs. 4(a)–4(c). We took the maximum amplitude projection (MAP) along the depth (or axial) direction to produce these images. In Fig. 4(a), the regular PA image PA_1 with probe-only detection rendered severely ring-shaped artifacts, which reveal the side-lobe problem in regular (linear) Bessel-beam PAM. Especially for RBCs 2 and 3 as labeled in Fig. 4(a), the side lobe signals significantly interfere with other main lobe signals. After irradiation by the heating laser, the PA signal PA_2 and thereby the signal-to-background ratio were enhanced owing to the GR effect, as indicated in Fig. 4(b), but the side lobe signals still exist. The maximum amplitude of PA_2 was 43% greater than that of PA_1 at the same position, which showed that there was a temperature rise of 13°C in the RBCs due to Grueneisen effect. According to this temperature rise, the effective optical fluence around the central lobe is estimated to be 195 mJ/cm^2.[27] In Fig. 4(c), the differential image ΔPA shows significantly reduced side lobe signals and reveals each RBC clearly with a higher signal-to-background ratio.
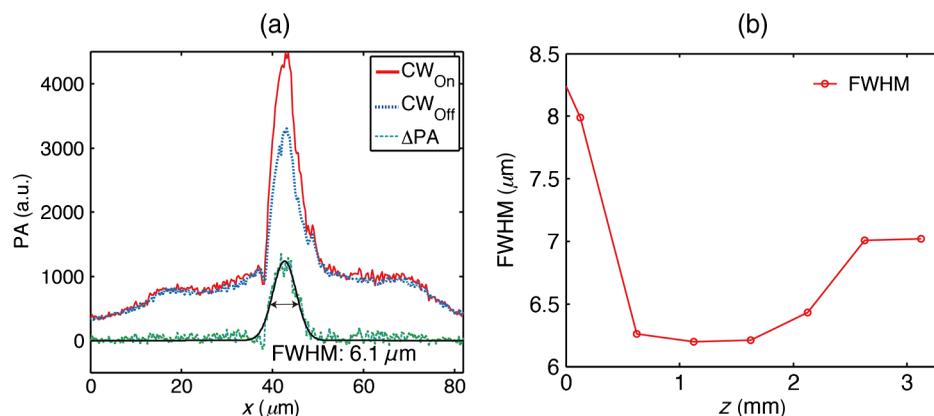

Fig. 3 Cross-sectional images of a 6-μm-diameter carbon fiber. (a) Red line: one-dimensional (1-D) photoacoustic (PA) image acquired when the CW laser is on. Blue line: 1-D PA image acquired when the CW laser is off. Green line: the differential PA image ΔPA. Black line: Gaussian fit of ΔPA. The FWHM of the ΔPA image is 6.1 μm. To improve SNR, 20 measurements were averaged. (b) Axial distribution of the FWHM of the cross-sectional carbon fiber images. The axial coordinate z is relative to the beginning measurement position ($z = 0$ is about 7 mm away from the tip of the axicon lens).
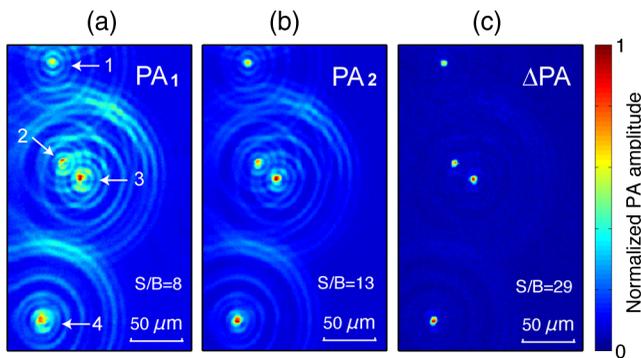
Fig. 4 Single-layer red blood cell (RBC) imaging. (a) Two-dimensional (2-D) PA image (PA$_1$) of four RBCs in agar medium. No heating laser was applied. (b) 2-D thermally enhanced PA image (PA$_2$) of the same RBCs. The probe laser, triggered at 300 ns after the release of pulsed heating laser shot, detected the PA signal. (c) 2-D differential PA image of the same RBCs. $\Delta PA = PA_2 - PA_1$. All images are normalized to the maximum amplitude of all pixels. There was no averaging for each image. (S/B: signal-to-background ratio).

Further, the nonlinear Bessel-beam PAM was used to image two thick RBC samples in agar medium. The first sample was 400-μm thick. Figure 5 shows the MAP images.[28] The maximal amplitude of each A-line at every pixel from 2-D raster scanning constitutes the MAP image, which can be interpreted as stacked images along the z-axis. A regular probe-only Bessel-beam PA MAP image of the 400-μm thick RBC sample is shown in Fig. 5(a), which is blurred due to the accumulation of side lobe signals. In addition, in this sample, some RBCs were separated from other cells, while others were aggregated. The side lobe signals from the big aggregated RBC clusters dominated over the main lobe signals of single RBCs or small aggregated RBC clusters, resulting in more artifacts than in the single-layer RBC sample. As a consequence, it is difficult to identify RBCs in Fig. 5(a). On the other hand, as shown in Fig. 5(b), the MAP of the nonlinear Bessel-beam image dramatically improved the image quality. The single or clustered RBCs in Fig. 5(b) can be clearly distinguished from the background. For example, comparing the lower-left corners of Figs. 5(a) and 5(b), we see a high background covering the actual main lobe signals in Fig. 5(a), while the background in Fig. 5(b) is dramatically reduced.

The second sample was 1-mm thick. Figure 6 shows the linear (PA$_1$) and nonlinear (ΔPA) Bessel-beam PA images
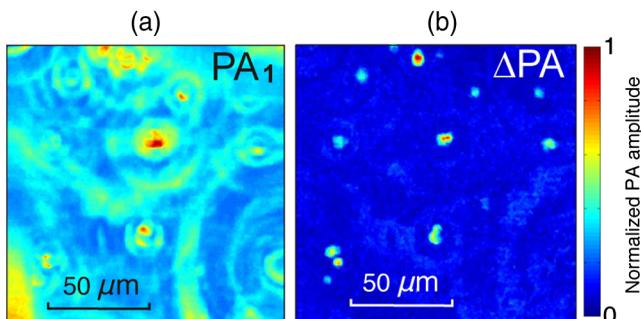

Fig. 5 2-D maximum amplitude projected (MAP) volumetric image of a 400-μm-thick RBC sample in agar medium. (a) Linear Bessel-beam PA image (PA$_1$) acquired without heating laser. (b) Nonlinear Bessel-beam PA image based on the differential PA image (ΔPA).
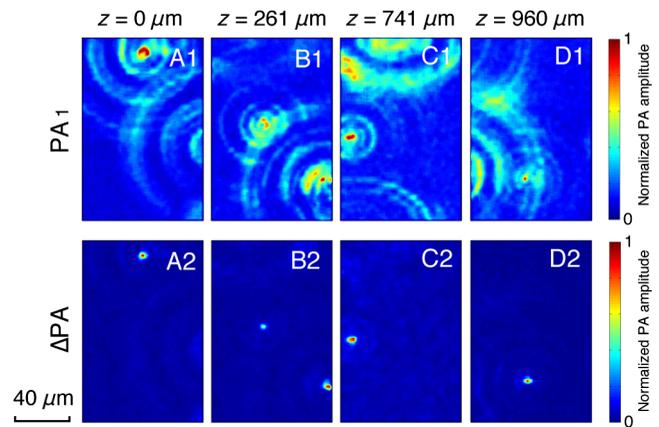

Fig. 6 2-D image slices from a volumetric image of a 1-mm-thick RBC sample in agar medium. Upper row: regular Bessel-beam PA images (PA$_1$). Lower row: nonlinear Bessel-beam PA images (ΔPA). Images at relative axial depths (a1 and a2) $z = 0$ μm, (b1 and b2) $z = 261$ μm, (c1 and c2) $z = 741$ μm, and (d1 and d2) $z = 960$ μm. The maximum signal amplitude was normalized to be 1 in each image.

obtained at different depths from $z = 0$ to 960 μm. Four sets of 2-D images were extracted from volumetric images of the sample. Comparing the linear (PA$_1$) and nonlinear (ΔPA) images, it is clear that the nonlinear approach was able to highlight central lobe signals and suppress the side-lobe background over a 1-mm depth. For example, the image in Fig. 6(d1) shows high background arising from side lobes, almost "burying" the actual signal from the main lobe, whereas the nonlinear image in Fig. 6(d2) clearly shows a clear main lobe signal. Deeper images were noisy and have weak nonlinear effects due to the limited effective focal depth of the Bessel beam in the current experimental setup. Compared with two-photon Bessel-beam microscopy,[10,25] nonlinear Bessel-beam PAM not only provides a similar long imaging depth but also provides axial resolution along the z-axis, which is determined by the bandwidth of the ultrasonic signal. In this system, the axial resolution is estimated as 30 μm.

5 Conclusions

In summary, we have demonstrated the extended imaging depth and optical lateral resolution of nonlinear Bessel-beam PAM in imaging carbon fibers and RBC samples. The imaging depth is determined by the effective depth of field of the Bessel beam, and the resolution is mainly determined by the central lobe diameter of the Bessel beam. In linear Bessel-beam PAM, the image quality is poor due to the side-lobe effect, whereas in nonlinear Bessel-beam PAM, the side lobe signals are effectively suppressed, thereby highlighting the main lobe signal and offering optical lateral resolution. The experimental system can be converted to reflective mode for *in vivo* imaging by following the design for previous OR-PAM systems.[1] Although the optical fluence used in this work (195 mJ/cm^2) is higher than the ANSI standard (20 mJ/cm^2) but lower than the damage threshold, improving the ultrasound transducer's sensitivity to increase the signal-to-noise ratio can reduce the optical fluence. Nonlinear Bessel-beam PAM effectively extends the focal depth of PA imaging beyond that of conventional Gaussian-beam PAM and therefore reduces the time to image thick samples.

Acknowledgments

References

1. K. Maslov et al., "Optical-resolution photoacoustic microscopy for *in vivo* imaging of single capillaries," *Opt. Lett.* **33**(9) 929–931 (2008).
2. L. V. Wang and S. Hu, "Photoacoustic tomography: *in vivo* imaging from organelles to organs," *Science* **335**(6075), 1458–1462 (2012).
3. L. Wang, K. Maslov, and L. V. Wang, "Single-cell label-free photoacoustic flowoxigraphy *in vivo*," *Proc. Natl. Acad. Sci. U. S. A.* **110**(15), 5759–5764 (2013).
4. L. V. Wang and L. Gao, "Photoacoustic microscopy and computed tomography: from bench to bedside," *Annu. Rev. Biomed. Eng.* **16**(1), 155–185 (2014).
5. J. Yao et al., "High-speed label-free functional photoacoustic microscopy of mouse brain in action," *Nat. Methods* **12**(5), 407–410 (2015).
6. J. Durnin and J. J. Miceli, "Diffraction-free beams," *Phys. Rev. Lett.* **58**(15), 1499–1501 (1987).
7. J. Durnin, J. J. Miceli, Jr., and J. H. Eberly, "Comparison of Bessel and Gaussian beams," *Opt. Lett.* **13**(2), 79–80 (1988).
8. M. R. Lapointe, "Review of non-diffracting Bessel beam experiments," *Opt. Laser Technol.* **24**(6), 315–321 (1992).
9. C. Kim et al., "Objective-free optical-resolution photoacoustic microscopy," *J. Biomed. Opt.* **18**(1), 010501 (2013).
10. E. J. Botcherby, R. Juškaitis, and T. Wilson, "Scanning two photon fluorescence microscopy with extended depth of field," *Opt. Commun.* **268**(2), 253–260 (2006).
11. T. A. Planchon et al., "Rapid three-dimensional isotropic imaging of living cells using Bessel beam plane illumination," *Nat. Methods* **8**(5), 417–423 (2011).
12. L. Gao et al., "Noninvasive imaging beyond the diffraction limit of 3D dynamics in thickly fluorescent specimens," *Cell* **151**(6), 1370–1385 (2012).
13. G. Thériault, Y. De Koninck, and N. McCarthy, "Extended depth of field microscopy for rapid volumetric two-photon imaging," *Opt. Express* **21**(8), 10095–10104 (2013).
14. G. Thériault et al., "Extended two-photon microscopy in live samples with Bessel beams: steadier focus, faster volume scans, and simpler stereoscopic imaging," *Front. Cell Neurosci.* **8**, 139 (2014).
15. G. Langer et al., "Two-photon absorption-induced photoacoustic imaging of Rhodamine B dyed polyethylene spheres using a femtosecond laser," *Opt. Express* **21**(19), 22410–22422 (2013).
16. Y. Yamaoka, M. Nambu, and T. Takamatsu, "Fine depth resolution of two-photon absorption-induced photoacoustic microscopy using low-frequency bandpass filtering," *Opt. Express* **19**(14), 13365–13377 (2011).
17. R. L. Shelton and B. E. Applegate, "Ultrahigh resolution photoacoustic microscopy via transient absorption," *Biomed. Opt. Express* **1**(2), 676–686 (2010).
18. S. P. Mattison and B. E. Applegate, "Simplified method for ultra high-resolution photoacoustic microscopy via transient absorption," *Opt. Lett.* **39**(15), 4474 (2014).
19. R. L. Shelton, S. P. Mattison, and B. E. Applegate, "Volumetric imaging of erythrocytes using label-free multiphoton photoacoustic microscopy," *J. Biophotonics* **7**(10), 834–840 (2014).
20. L. Wang, C. Zhang, and L. V. Wang, "Grueneisen relaxation photoacoustic microscopy," *Phys. Rev. Lett.* **113**(17), 174301 (2014).
21. A. Danielli and K. Maslov, "Label-free photoacoustic nanoscopy," *J. Biomed. Opt.* **19**(8), 086006 (2014).
22. G. Indebetouw, "Nondiffracting optical fields: some remarks on their analysis and synthesis," *J. Opt. Soc. Am. A* **6**(1), 150–152 (1989).
23. G. Scott, "Efficient generation of nearly diffraction-free beams using an axicon," *Opt. Eng.* **31**(12), 2640–2643 (1992).
24. O. Brzobohatý, T. Cižmár, and P. Zemánek, "High quality quasi-Bessel beam generated by round-tip axicon," *Opt. Express* **16**(17), 12688–12700 (2008).
25. G. Thériault, Y. De Koninck, and N. McCarthy, "Extended depth of field microscopy for rapid volumetric two-photon imaging," *Opt. Express* **21**(8), 10095–10104 (2013).
26. L. V. Wang and H. Wu, *Biomedical Optics: Principles and Imaging*, John Wiley & Sons, Hoboken, New Jersey (2012).
27. P. Lai et al., "Photoacoustically guided wavefront shaping for enhanced optical focusing in scattering media," *Nat. Photonics* **9**(2), 126–132 (2015).
28. H. F. Zhang, K. Maslov, and L. V. Wang, "*In vivo* imaging of subcutaneous structures using functional photoacoustic microscopy," *Nat. Protoc.* **2**(4), 797–804 (2007).

Junhui Shi received his BSc in chemical physics from the University of Science and Technology of China. Then, he continued to study chemistry and received his PhD at Princeton University, Princeton, New Jersey. He was working on theoretical chemical dynamics and experimental nuclear magnetic resonance spectroscopy. Currently, he is working on photoacoustic imaging in the biomedical engineering department at Washington University in St. Louis, Missouri.

Lidai Wang received his bachelor's and master's degrees from the Tsinghua University and received his PhD degree from the University of Toronto. After working as a postdoctoral research fellow at Washington University in St. Louis, he joined the City University of Hong Kong as an assistant professor in 2015. His research focuses on biophotonics, biomedical imaging, wavefront engineering, instrumentation, and their biomedical applications.

Cedric Noordam studies physics and biomedical engineering at the University of Twente, The Netherlands. He will receive his Master of Science degree in the fall of 2015. He did an internship at the Optical Imaging Lab at Washington University in St. Louis, where he did research on photoacoustics. His research interests include plasmonics, surface enhanced Raman spectroscopy, nano-optics, photoacoustics, and optics in general with biomedical applications.

Lihong V. Wang is the Beare distinguished professor at Washington University. His book titled *Biomedical Optics* won the Goodman Award. He has published 420 journal articles with an h-index of 99 (>30,000 citations) and delivered 400 keynote/plenary/invited talks. His laboratory published first functional photoacoustic CT, three-dimensional photoacoustic microscopy and compressed ultrafast photography. He serves as the editor-in-chief of the *Journal of Biomedical Optics*. He was awarded OSA's C.E.K. Mees Medal, NIH Director's Pioneer Award, and IEEE's Biomedical Engineering Award.